The Astrophysical Journal, 928:78 (13pp), 2022 March 20 https://doi.org/10.3847/1538-4357/ac5117

Subaru/Hyper Suprime-Cam z-Broadband Excess Selection of Extreme Emission Line Galaxies at $z < 1$

Benjamin E. Rosenwasser[1], Anthony J. Taylor[1], Amy J. Barger[1,2,3], Lennox L. Cowie[3], Esther M. Hu[3], Logan H. Jones[1,4], and Antoinette Songaila[3]
[1] Department of Astronomy, University of Wisconsin–Madison, 475 N. Charter Street, Madison, WI 53706, USA; ataylor@astro.wisc.edu
[2] Department of Physics and Astronomy, University of Hawaii, 2505 Correa Road, Honolulu, HI 96822, USA
[3] Institute for Astronomy, University of Hawaii, 2680 Woodlawn Drive, Honolulu, HI 96822, USA
[4] Space Telescope Science Institute, 3700 San Martin Drive, Baltimore, MD 21218, USA
Received 2021 October 25; revised 2022 January 19; accepted 2022 January 24; published 2022 March 28

Abstract

We present a search for extreme emission line galaxies (EELGs) at $z < 1$ in the COSMOS and North Ecliptic Pole (NEP) fields with imaging from Subaru/Hyper Suprime-Cam (HSC) and a combination of new and existing spectroscopy. We select EELGs on the basis of substantial excess flux in the z broad band, which is sensitive to Hα at $0.3 \lesssim z \lesssim 0.42$ and [O III]λ5007 at $0.7 \lesssim z \lesssim 0.86$. We identify 10,470 galaxies with $z$excesses in the COSMOS data set and 91,385 in the NEP field. We cross-reference the COSMOS EELG sample with the zCOSMOS and DEIMOS 10k spectral catalogs, finding 1395 spectroscopic matches. We made an additional 71 (46 unique) spectroscopic measurements with $Y < 23$ using the HYDRA multiobject spectrograph on the WIYN 3.5 m telescope, and 204 spectroscopic measurements from the DEIMOS spectrograph on the Keck II telescope, providing a total of 1441/10,470 spectroscopic redshifts for the EELG sample in COSMOS (∼14%). We confirm that 1418 (∼98%) are Hα or [O III]λ5007 emitters in the above stated redshift ranges. We also identify 240 redshifted Hα and [O III]λ5007 emitters in the NEP using spectra taken with WIYN/HYDRA and Keck/DEIMOS. Using broadband-selection techniques in the $g - r - i$ color space, we distinguish between Hα and [O III]λ5007 emitters with 98.6% accuracy. We test our EELG selection by constructing Hα and [O III]λ5007 luminosity functions and comparing to recent literature results. We conclude that broadband magnitudes from HSC, the Vera C. Rubin Observatory, and other deep optical multiband surveys can be used to select EELGs in a straightforward manner.

Unified Astronomy Thesaurus concepts: Emission line galaxies (459); Broad band photometry (184); Galaxy evolution (594)

Supporting material: machine-readable table

1. Introduction

Emission line galaxies (ELGs) are direct tracers of star formation throughout cosmic time. Understanding the evolution of their properties, such as their number density, fluxes, and line ratios is a major observational effort. ELGs have remained a topic of great interest since they were first investigated in detail (e.g., Zwicky 1964; Sargent 1970; Sargent & Searle 1970). ELGs have low stellar masses and metallicities, and they have been used as the basis for searches for the lowest metallicity and/or youngest galaxies and for Lyman continuum leakers and analogs of galaxies that reionized the universe (e.g., Izotov & Thuan 2016; Izotov et al. 2021; Naidu et al. 2022; Tang et al. 2021; I. Laseter et al. 2022, in preparation). Additionally, ELGs are used as cosmological distance probes using the L–σ relation (González-Morán et al. 2019). Their relevance to galaxy evolution is not limited to these examples.

Decades of research on this heterogeneous class have led to numerous naming conventions including the following: H II galaxies (Sargent & Searle 1970), Blue Compact Dwarfs (BCDs; Thuan & Martin 1981), Ultrastrong ELGs (USELs; Kakazu et al. 2007), Green Peas (Cardamone et al. 2009), Luminous Compact Galaxies (LCGs; Izotov et al. 2011), Extreme ELGs (EELGs; Amorín et al. 2015; Tanaka et al. 2022), Star-forming Dwarf Galaxies (SFDG; Grossi 2018), and even Lyman Break Galaxies (LBGs) by the high-redshift ($z \sim 3$) IRAC studies (e.g., Magdis et al. 2008). The lack of consensus on a naming convention may reflect the rather small size (∼hundreds) of the current spectroscopically confirmed known population.

This class of galaxy is usually selected using the equivalent widths (EWs) of the Hα and [O III]λ5007 lines. We will refer to these galaxies as EELGs in reference to their extreme EWs. EELGs are easy to identify in grism observations (Atek et al. 2011; Maseda et al. 2018; Boyett et al. 2021), which have confirmed a steep positive evolution in their number density from the local value to higher redshifts (Noeske et al. 2006). More recent studies have used slit-based spectroscopy to push these measurements to redshift $z \approx 7$ and beyond (Endsley et al. 2021). The upcoming near-infrared (NIR) grism missions Euclid and the Nancy Grace Roman Space Telescope (RST) should detect the full population of these galaxies selected by Hα emission at $0.7 < z < 2.05$ and by [O III]λ5007 emission at $1.2 < z < 3$ over tens of thousands of square degrees. The Near-Infrared Imager and Slitless Spectrograph (NIRISS) on the James Webb Space Telescope will extend these sensitivities to $z \approx 0.2$ and $z \approx 0.6$, respectively, but its comparatively small $2\farcm2 \times 2\farcm2$ field of view may limit its usefulness for wide-field EELG surveys.

When extending the large-volume studies of EELGs to lower redshifts where the emission lines of interest are in the optical regime, the NIR grism technique is not applicable. Wide-field optical selections at $z \leqslant 1$ have typically relied on narrowband imaging, which can be done over large areas (Hayashi et al. 2018) but in only relatively small volumes due to the intrinsic narrow bandwidth of such filters, which results in a narrow redshift range. Hyper Suprime-Cam (HSC; Miyazaki et al. 2012) on the Subaru 8.2 m telescope, for example, has mapped ∼hundreds of square degrees in narrowbands with the largest contiguous area being the North Ecliptic Pole (NEP; A. Taylor et al. 2022, in preparation). The Vera C. Rubin Observatory (VRO), will conduct the only deep and wide-area optical survey comparable in sky coverage to the NIR missions, but the telescope will be equipped with 6 broadband filters (*ugrizY*) and no narrowband filters. Thus, any future selection of VRO-EELG sources will be limited to broad bands.

Techniques employing wider filters have been used to find EELGs at a variety of redshifts. At $z \leqslant 0.3$, both intermediate-band filters (Hinojosa-Goñi et al. 2016; Lumbreras-Calle et al. 2019) and broadband filters (Cardamone et al. 2009; Yang et al. 2017) have been employed. Broadband filters have also been used in the optical to locate intermediate-redshift ($z \sim 0.5$) samples (Li & Malkan 2018) and in the NIR to locate high-redshift ($z \geqslant 1.0$, van der Wel et al. 2011; Huang et al. 2015; Tang et al. 2019) and very high-redshift ($4 \leqslant z \leqslant 8$, Smit et al. 2015) samples. Current broadband-selected samples in the optical have used relatively shallow SDSS imaging (Cardamone et al. 2009; Yang et al. 2017; Li & Malkan 2018).

The use of broadband filters when compared to narrowband filters for EELG selection offers several benefits as well as a number of challenges. The most immediate benefit is the larger volume probed by broadband filters, which is typically roughly proportional to the filter width at a fixed central redshift. These larger volumes allow for proportionally larger detected samples of EELGs per unit area on the sky. The cost of this larger volume is an increase in uncertainty in the redshifts of the detected sources, as the detected emission line of interest may generally lie anywhere within the broadband-filter passband. Additionally, the sensitivity of a filter, to emission line detections at a fixed EW using a narrowband- or broadband-excess technique, is generally inversely proportional to the filter width; thus, narrowband filters have better sensitivity to lower-EW sources than broadband filters.

In this work, we select EELGs in the COSMOS and NEP fields using deep HSC imaging in five optical bands (*grizY*). We focus on redshifts $z \leqslant 1$, which are out of the range of Euclid and RST. We look for excess flux in the *z*band relative to the *i*band and *Y*band, which is sensitive to Hα from $0.3 \leqslant z \leqslant 0.42$ and [O III] λ5007 from $0.7 \leqslant z \leqslant 0.86$, and we use the $g - r - i$ broadband color space to separate these two subsamples. We assume $\Omega_M = 0.3$, $\Omega_\Lambda = 0.7$, and $H_0 = 70\,\mathrm{km\,s^{-1}\,Mpc^{-1}}$ throughout. All magnitudes are provided in the *AB* magnitude system, where an *AB* magnitude is defined by $m_{AB} = -2.5 \log f_\nu - 48.60$, and f_ν, the flux of the source, is given in units of $\mathrm{erg\,cm^{-2}\,s^{-1}\,Hz^{-1}}$.

2. Three-filter Broadband Selection

Our COSMOS magnitudes come from the Hyper Suprime-Cam Subaru Strategic Program DR3 (HSC-SSP PDR3; see details in Aihara et al. 2022). We use the COSMOS Deep and UltraDeep data sets, and we select a subregion covering 3.15 deg^2. This catalog contains 1,531,398 detected sources.

Our NEP imaging data come from the Hawaii EROsita Ecliptic pole Survey (HEROES) and consist of 34.2 deg^2 of deep *grizY* broadband and NB816, NB921 narrowband imaging. While the HEROES narrowband imaging has been used extensively for selecting ultraluminous Lyα emitters at $z > 5$ (Songaila et al. 2018; Taylor et al. 2020, 2021), in this work we focus on the survey's broadband-selection potential.

The full details on the observations and data reduction for HEROES are given in Songaila et al. (2018). Briefly, the HEROES imaging was processed using the Pan-STARRS Image Processing Pipeline (IPP; Magnier et al. 2020a, 2020b). The IPP was also used for source detection. Sources were added to the master catalog with both Kron and forced aperture magnitudes for all 7 filters, if a source were detected at 5σ in any one of the 7 filters. The full HEROES catalog consists of ∼24 million sources, with 91,385 potential *z*-excess EELG candidates. The 1σ noise in corrected $2''$ diameter apertures in each broad band are *g*: 27.79, *r*: 27.07, *i*: 27.02, *z*: 26.66, and *Y*: 24.71.

Broadband selection in the optical based on strong [O III]λ5007 emission has been performed at low redshift by Cardamone et al. (2009) in the *r*band and by Li & Malkan (2018) in the *i*band. Here we perform a similar selection using the *z*band, and we look for an excess relative to the neighboring *i* and *Y*bands. This selection traces [O III]λ5007 emission in the redshift range $0.7 \lesssim z \lesssim 0.86$, and H$\alpha$ emission at $0.3 \lesssim z \lesssim 0.42$. Using a *z*excess has the advantage of tracing EELGs in two redshift ranges in which they appear in significant numbers, while *r* and *i* are sensitive to only [O III]λ5007-emitters at lower redshifts.

In Figure 1, we show our color–color selection of EELG candidates. In both fields, we measured $3''$ diameter magnitudes at the positions of all the catalog sources in each survey's stacked imaging to ensure consistent magnitude measurements between the two fields. We then selected the sources with the brightness cuts of *g*, *r*, *i*, $z < 25$, and $Y < 23$, corresponding to $\gtrsim 5\sigma$ detections in all five broad bands, to ensure clean detections in *Y*. We next applied principal color cuts of $z - Y < 0.0$ and $i - z > 0.17$. We imposed an additional color cut of $(i - z) + 2(z - Y) < 0.3$ to reject sources with simultaneous extreme $(i - z)$ colors and moderate $(z - Y)$ colors, which are more indicative of Balmer break galaxies at redshift $z \sim 1.4$ or LBGs at $z > 6$ than of EELGs at redshift $z < 1$.

We applied the same cuts to both HEROES and COSMOS, as both fields share similar distributions of sources in the $i - z - Y$ space. In this color–color space, the EELG candidates form a substantial outcropping not seen in other color–color spaces (such as the $r - i - z$ space used by Li & Malkan 2018). We also used the HEROES imaging to measure the FWHM of the brightness profile of each source in the *z*band. We used these data to reject overly compact stellar contaminants and cosmic rays as a function of both FWHM and *z*-filter excess: FWHM $< 0''.6$–$0.1((i+y)/2-z)$. We calibrated this cut using the FWHM data in conjunction with our spectroscopic follow-up (see Section 3 below). The combination of all of these cuts produced our *z*-excess sample.

While both fields use HSC imaging, the Deep/UltraDeep COSMOS data are of significantly higher quality than HEROES. This may be due in part to the superior cosmic ray rejection and stacking routines in `HSCPIPE` (Bosch et al. 2018, 2019) used to produce the HSC-SSP imaging data and catalogs. As a result, the scatter in the HEROES color–color diagrams is significantly increased compared to the analogous

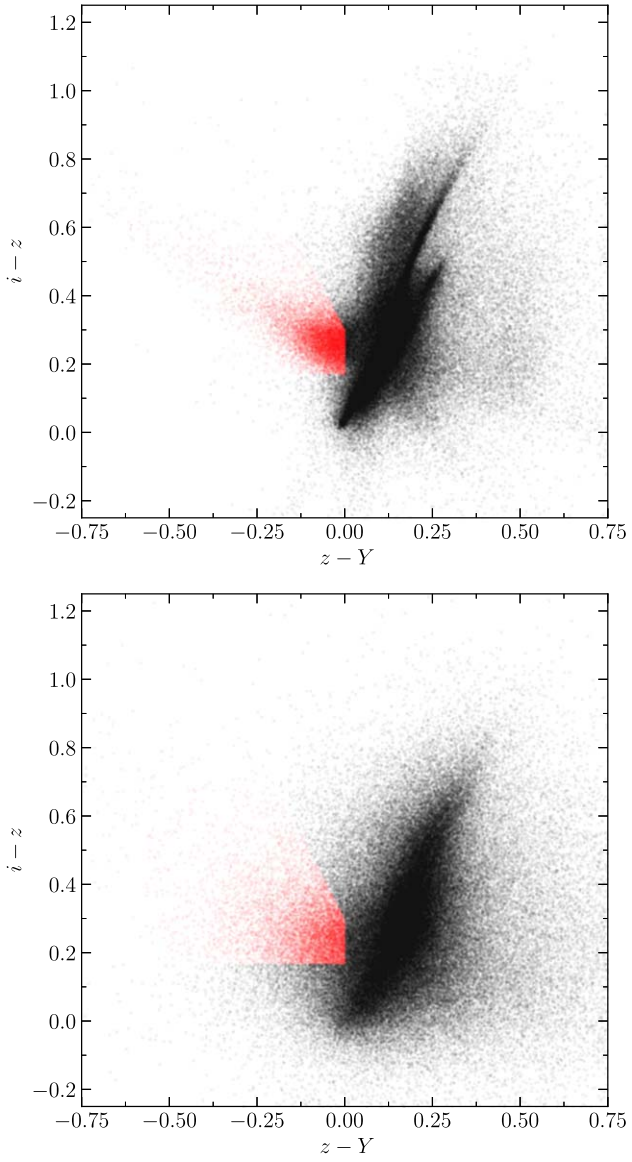

Figure 1. Top: $i-z$ vs. $z-Y$ colors for the COSMOS HSC-SPP catalog. The small black points are the full HSC-SPP catalog with g, r, i, $z<25$, and $Y<23$ while the red points are the z-excess sample under study. The z-excess galaxies form a substantial outcropping. Bottom: same as above for the HEROES catalog. Note that, due to the large ∼34 deg^2 area, only 11% of the full catalog sources are plotted to match the COSMOS field size. Due to the superior stacking pipeline and imaging depth in COSMOS HSC-SSP, some finer $i-z-Y$ color space features are less resolved in the HEROES catalog.

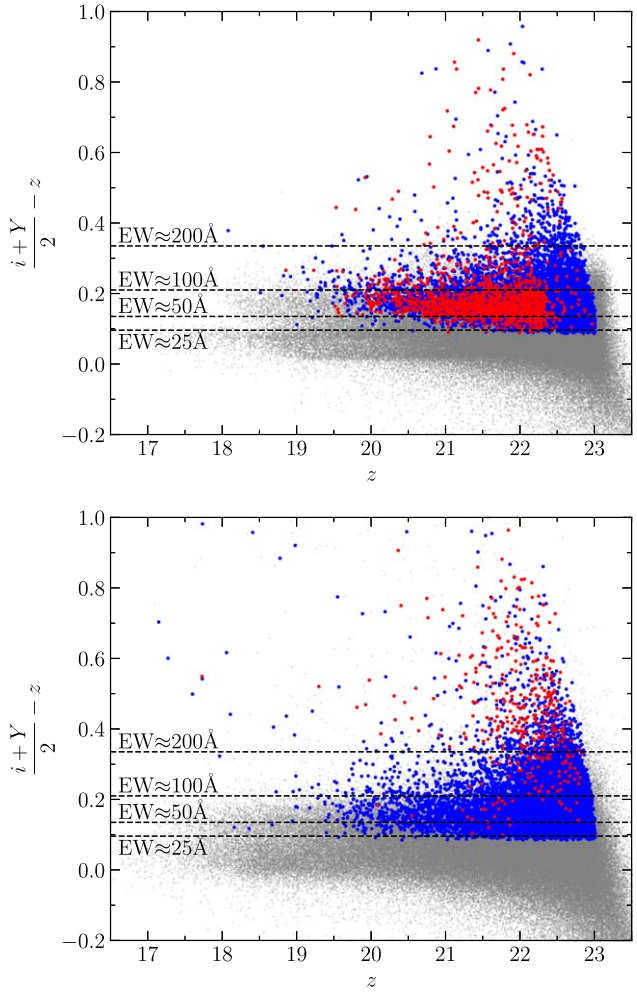

Figure 2. $(i+Y)/2-z$ vs. z-broadband-excess-magnitude diagrams for COSMOS (top) and HEROES (bottom). The small gray points are the full HSC catalog, the blue points are the z-excess photometric sample, and the red points indicate galaxies in our sample with observed spectroscopic redshifts. Note that, to avoid overcrowding, only 11% of the full HEROES photometric catalog is plotted. The dashed lines are lines of approximate Hα or [O III]λ5007 observed-frame EWs.

COSMOS diagrams. We are currently remastering HEROES using a combination of new and archival imaging with `HSCPIPE` for use in future work (A. Taylor et al. 2022, in preparation).

In Figure 2, we plot $(i+Y)/2-z$ color excess versus z magnitude, with small gray points showing our full COSMOS and HEROES catalogs, blue points showing the photometric z-excess samples, and red points marking sources in the photometric z-excess samples with spectroscopic redshifts (discussed below). The z-excess samples have a minimum $z$excess of 0.085, which corresponds to an estimated observed-frame Hα or [O III]λ5007 line EW of ∼20 Å. The median $z$excess is ∼0.18, corresponding to an estimated observed-frame Hα or [O III]λ5007 line EW of ∼70 Å and thus classifying these as EELGs (e.g., Amorín et al. 2015). We discuss the calculation and distribution of EWs further in Section 5.2. We plot lines of the constant estimated observed-frame EW in Figure 2 as black dashed lines.

Our final z-excess samples consist of 10,470 sources in COSMOS and 91,385 in HEROES.

3. Spectroscopic Redshifts

In order to characterize the z-excess selection for use with existing and future multiband catalogs, we calibrated the photometric selection above using newly observed and archival spectroscopic redshifts. First, we matched our COSMOS photometric sample to three spectroscopic surveys in the COSMOS field: zCOSMOS Bright 20k (Lilly et al. 2009), DEIMOS 10k (Hasinger et al. 2018), and our WIYN-targeted samples (described below). We obtained 1245 matches from zCOSMOS, 204 from DEIMOS, and 71 from WIYN, for a total of 1520 redshifts (1441 unique), or 13.8% spectroscopic completeness.

The spectroscopic coverage provided by zCOSMOS only probes to $i\sim22.5$, much shallower than the HSC imaging. In order to probe the fainter magnitudes probed by the COSMOS HSC imaging, we performed additional spectroscopic follow-up

for a small number of COSMOS sources with $Y \lesssim 23$ using the multiobject spectrograph HYDRA on the 3.5 m WIYN telescope at Kitt Peak National Observatory. The observations were made in a series of runs in 2016 January, February, and March that targeted both broadband- and narrowband-excess candidates. We used HYDRA's "red" fiber bundle that is optimized for 5000–9500 Å throughput and contains ∼80 fibers with 2″.0 diameters and a positional accuracy of 0″.3. About 10 fibers per configuration were placed in random sky locations and combined to produce an average sky spectrum. We configured the spectrograph using the 316@7.0 grating and GG-420 filter, providing a spectral resolution of 2.6 Å pixel^{-1}. Second-order contamination did not appear to affect our redshift measurements. Calibrations were done for each configuration with a CuAr lamp. The reduction was carried out with standard IRAF routines for dark and bias subtraction and flat-fielding, and the IRAF task `dohydra` was used for sky subtraction and dispersion calculation. Redshifts were measured by eye on the basis of the strong emission lines and were later refined through spectral fitting, using the by-eye redshifts as initial guesses for the fitter (see Section 5.1). Based on the 2.6 Å pixel^{-1} spectral resolution, we estimate our 1σ redshift errors at ± 0.002. We obtained redshifts for 71 total sources from the photometric sample, 46 of which had not been previously measured in other surveys.

We plot all spectroscopically observed sources in $i-z-Y$ color space in Figure 3 (top). Note that the sources that we observed with WIYN tended to have larger $z$excesses than the more generally selected targets of zCOSMOS and DEIMOS 10K. This selection bias was by design, both to better sample the $i-z-Y$ color–color space and to search for high-EW EELGs.

After verifying the success of the $i-z-Y$ selection in COSMOS, we used the same HYDRA configuration to observe sources in the spectroscopically unexplored NEP during runs in 2017 June, 2017 October, 2018 May, and 2018 September. In total, we observed 331 candidates and obtained redshifts for 240 (73%) of them. Many of the remaining 91 sources showed blank spectra with no discernible emission lines or features. Upon further inspection, around a third of these sources also showed nearby noise and neighboring sources in the HSC imaging.

We supplemented our catalog of WIYN/HYDRA spectra with sources from various Keck/DEIMOS runs that had narrowband selected Lyα emitters at $z > 5$ as the primary targets (Hu et al. 2016; Songaila et al. 2018; Taylor et al. 2020, 2021). This catalog contains spectroscopic redshifts for 1191 objects at $z < 6.6$. Of these, 33 match candidates in the z-excess sample for a total of 364 (357 unique) redshifts in HEROES.

Due to the large area of HEROES, this represents only a small fraction 357/91,385 (0.39%) of the identified z-excess candidates. However, the total (HYDRA+DEIMOS) sample of 357 spectroscopically identified candidates is sufficient as a sample of HEROES EELGs and as further verification that the $i-z-Y$ selection methods work. We plot this sample of spectroscopic sources in Figure 3 (bottom). Note that as in COSMOS, the HYDRA spectra sample a much more extreme color–color space than the narrowband selected DEIMOS spectra. This is again by design, as we were interested in searching for particularly strong EELG sources.

In Figure 4, we show the distribution of redshifts for the spectroscopically observed z-excess objects in both fields. The dashed black profiles correspond to the z-filter transmission at the redshifts where Hα and [O III]λ5007 are within the z passband. The redshift distribution is highly peaked in the two redshift ranges

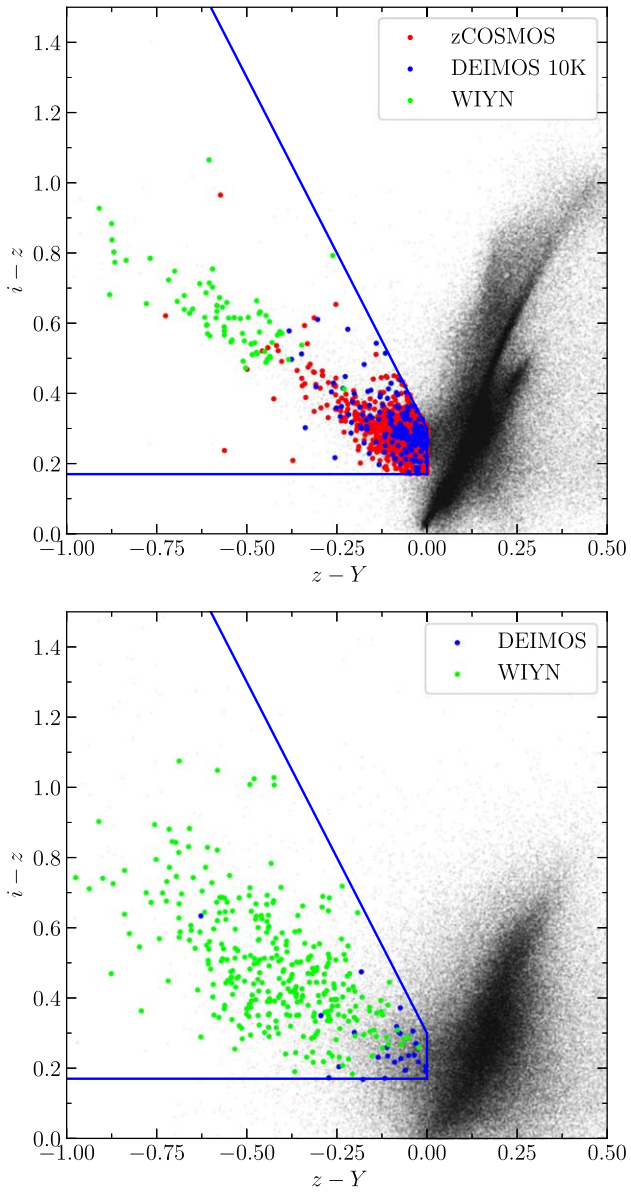

Figure 3. The spectroscopic samples in COSMOS (top) and HEROES (bottom) plotted in $i-z-Y$ color–color space. Fine black points show the entire photometric catalogs, while red points show spectroscopic matches from zCOSMOS, blue points from DEIMOS, and green points from HYDRA. The $i-z-Y$ color selection cuts are shown by the blue borders.

defined by Hα and [O III]λ5007, $0.30 \lesssim z \lesssim 0.42$ and $0.7 \lesssim z \lesssim 0.86$. The bimodal shape of the distribution of [O III] emitters in COSMOS results from a combination of effects. Hasinger et al. (2018) noted this structure in the full DEIMOS 10K Bright survey and identified a protocluster and several filaments that caused the overdensity of sources at redshifts $z \approx 0.73$ and $z \approx 0.84$. Coincidentally, the peak at redshift $z \approx 0.84$ also corresponds to [O III]λ5007 entering a NB921 narrowband. As some of our WIYN/HYDRA objects were selected with narrowband imaging for use in other projects, these sources further accentuate the bimodal structure. The narrowband selection of DEIMOS sources in the NEP causes the same effect to a lesser extent.

1679/1789 galaxies (94%) fall in the two redshift ranges defined by redshifted Hα and [O III]λ5007 emission, while the remaining 110 are outside of these ranges, of which 107 showed

Table 1
Selected Spectroscopic Redshifts

Field	R.A. (J2000)	Decl. (J2000)	g	r	i	z	Y	Redshift	Instrument
COSMOS	149.27763	2.04143	22.56	22.28	22.12	21.44	22.31	0.717	HYDRA
COSMOS	149.29378	2.27055	23.79	23.46	23.04	22.49	22.92	0.847	HYDRA
COSMOS	149.35527	2.55651	23.50	23.26	22.93	22.29	22.94	0.820	HYDRA
COSMOS	149.50330	1.78595	23.44	23.17	22.86	22.39	22.89	0.789	HYDRA
COSMOS	149.52539	1.94894	22.43	21.94	22.08	21.51	21.91	0.371	HYDRA
COSMOS	149.63052	2.38696	23.06	22.54	22.81	22.27	22.75	0.339	HYDRA
COSMOS	149.70924	1.44678	23.04	22.82	22.58	21.96	22.58	0.788	HYDRA
COSMOS	149.72950	2.49113	23.04	22.99	22.90	22.12	22.99	0.832	HYDRA
COSMOS	149.77736	1.44253	22.44	22.22	21.95	21.38	21.89	0.784	HYDRA
COSMOS	149.81691	2.33237	23.37	22.99	22.62	22.06	22.60	0.761	HYDRA
…	…	…	…	…	…	…	…	…	…
NEP	273.68683	65.39443	22.93	22.89	22.66	22.03	22.65	0.846	DEIMOS
NEP	273.70792	67.62094	23.18	22.68	22.87	22.30	22.54	0.312	HYDRA
NEP	273.95770	67.06726	23.20	22.62	22.40	22.11	22.25	0.352	HYDRA
NEP	274.22275	67.21378	23.04	22.74	22.44	21.97	22.29	0.744	HYDRA
NEP	274.25754	68.67712	22.59	22.19	22.10	21.70	22.12	0.366	HYDRA
NEP	274.26724	68.24654	22.87	22.74	22.29	21.96	22.23	0.837	HYDRA
NEP	274.30870	67.60469	23.03	22.35	22.86	22.22	22.70	0.360	HYDRA
NEP	274.32544	68.20570	22.92	22.87	22.84	21.96	22.67	0.780	HYDRA
NEP	274.42224	67.83610	22.81	22.66	22.09	21.79	21.86	0.815	DEIMOS
NEP	274.42390	67.76432	22.48	22.02	21.79	21.57	21.59	0.313	DEIMOS

(This table is available in its entirety in machine-readable form.)

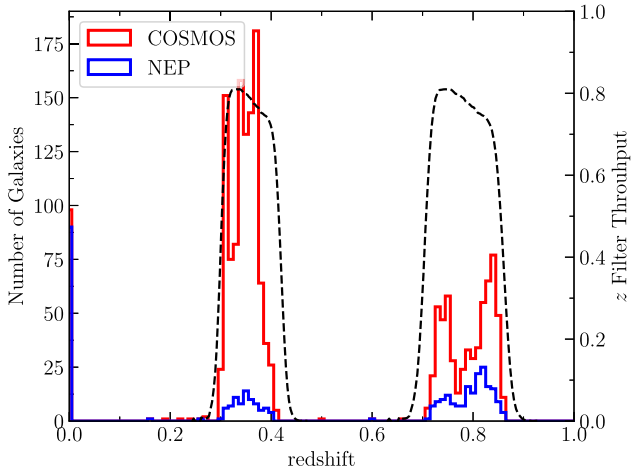

Figure 4. Stacked redshift distribution of the 1441 z-excess objects in COSMOS (red) and 357 in HEROES (blue) that were spectroscopically observed. The dashed black profiles correspond to the redshifts where Hα and [O III]λ5007 are within the z-filter passband. Sources with spectroscopic follow-up but no discernible spectral features and no evident redshift are assigned a redshift of $z = 0$ in this figure.

blank or indeterminate spectra. We thus confirm that the selection is primarily sensitive to Hα-emitters (HAEs) and [O III]λ5007-emitters (O3Es) at $0.3 \lesssim z \lesssim 0.42$ and $0.7 \lesssim z \lesssim 0.86$, respectively. Hereafter, when referring to HAEs or O3Es, we also imply that each species lies in these redshift bounds, and that [O III] refers to [O III]λ5007 unless otherwise stated. Our 94% overall sample purity is very comparable to the purities seen in narrowband surveys at similar redshifts, e.g., 95% for Hα at $z = 0.84$ (Sobral et al. 2013), 93.7% for Hα at $z = 0.47$, and 90.4% for [O III] at $z = 0.93$ (Khostovan et al. 2020). We summarize our spectroscopically confirmed HAEs and O3Es in Table 1.

4. Five-filter Broadband Selection

While the $i - z - Y$ broadband-selection method is a reliable method to construct large samples of HAEs and O3Es in a large volume and to faint magnitudes, it fails to distinguish between the two. However, HAEs and O3Es can be separated using the $g - r - i$ color–color space, primarily due to redshift dependent line contamination in the $r$band (see below). We demonstrate this method for each field in the upper plots of Figure 5, where we show $g - r$ versus $r - i$ for the sample of all photometric EELG candidates (black points), spectroscopically confirmed HAEs (red points), and spectroscopically confirmed O3Es (blue points). Ly et al. (2007) demonstrated a similar method, using $B - R_C - i'$ to distinguish HAEs from O3Es in NB921 (which overlaps the z filter) excess sources (see Ly et al. 2007, their Figure 7).

In Figure 5, the populations of HAEs and O3Es are separated into two distinct regions, characterized primarily by the strength of the $r$excess. There are multiple explanations for this effect. At redshifts $0.3 < z < 0.42$ where the Hα line falls in the z filter, the [O III] doublet happens to lie in r, exiting r at redshift $z \approx 0.42$. Thus, as long as Hα falls in z, a corresponding [O III] doublet will fall in r and will show an $r$excess relative to g and i. This separation might also be partially caused by continuum effects. Regardless of the underlying mechanism, the HAE population is cleanly observationally separated from the O3E sample in both fields.

The lower plots of Figure 5 further illustrate this effect, showing $r$excess $(\frac{g+i}{2} - r)$ versus r. It is clear that HAEs and O3Es can be distinguished from one another in 1410/1418 (99.4%, COSMOS) and 244/261 (93.9%, HEROES) of cases with an $r$excess that HAEs will exceed and O3Es will fall below. In each of our fields, this r-excess value corresponded to 0.12 mag.

Combining these conditions with the initial $i - z - Y$ cuts yields the following color criteria for HAE and O3E broadband identification:

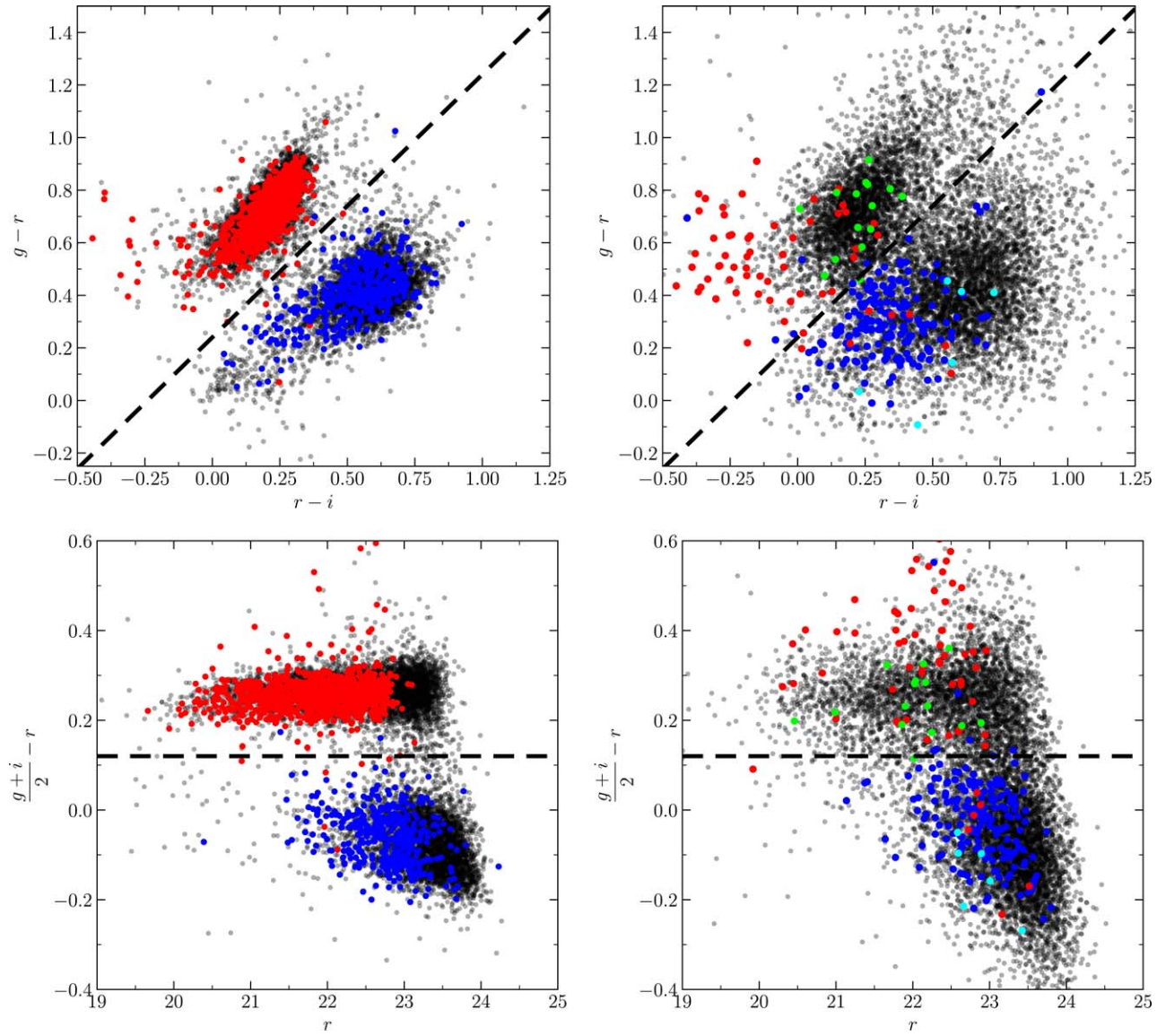

Figure 5. Upper left: $g - r - i$ plotted for COSMOS. Upper right: $g - r - i$ plotted for HEROES. Lower left: *r*excess vs. r plotted for COSMOS. Lower right: *r*excess vs. r plotted for HEROES. In all panels, red points are spectroscopic HAEs, blue points are spectroscopic O3Es, and translucent black points are photometric candidates. The black dashed lines represent an *r*excess of 0.12 mag. This is the optimal separation criterion for the two populations in each field. In HEROES (right-hand panels), the DEIMOS-identified HAEs are denoted by green points, and the DEIMOS-identified O3Es are denoted by cyan points. Note that the sources targeted in HEROES with HYDRA (blue and red points) tend to be bluer than the DEIMOS sources. This phenomenon is due to the deliberate selection of apparently extreme sources in the early stages of this work for HYDRA observations. The DEIMOS sources—originally selected based on narrowband excesses—are better centered on the populations of photometric candidates.

For HAEs at $0.3 \lesssim z \lesssim 0.42$, the following criteria are identified: $\frac{g+i}{2} - r > 0.12$, $i - z > 0.17$, $z - y < 0.00$, and $(i - z) + 2(z - y) < 0.30$.

And for O3Es at $0.7 \lesssim z \lesssim 0.86$, the following criteria are identified: $\frac{g+i}{2} - r < 0.12$, $i - z > 0.17$, $z - y < 0.00$, and $(i - z) + 2(z - y) < 0.30$.

These color cuts yield final photometric samples of 6211 HAEs and 4259 O3Es in COSMOS, and 39,109 HAEs and 52,276 O3Es in HEROES. From these photometric source counts, it is evident that the ratio of HAEs to O3Es is a factor of $\sim$2 higher in COMSOS than in HEROES. We attribute this discrepancy to cosmic variance (see also Section 5.6) and to differences in the data quality and photometric calibration between the two data sets.

5. Luminosity Functions

5.1. Line Fluxes and Luminosities

Using our samples of photometric HAEs and O3Es, we next construct luminosity functions (LFs) for each to test our selection in comparison to analogous narrowband studies. We use the broadband excess to calculate the line luminosity for each source —much like how a narrowband magnitude is used with an overlapping broadband measurement—to derive a line luminosity (e.g., Matthee et al. 2015, Equation (3)). In our broadband calculation, we estimate the continuum flux density in our central filter (z) by taking the average of the flux densities in the neighboring broadband filters (i and Y). We then assume that the difference (excess) between the measured z flux and the estimated

continuum flux is due to the emission line of interest and other nearby emission lines. From this excess, we derive the emission line fluxes and luminosities using our spectroscopic redshifts and the filter transmission curve.

We show the full derivation of the expression for the Hα luminosity in the Appendix. In brief, we consider the relative contributions of flux in *i*, *z*, and *Y* from Hα and [S II]λ6716,6731 as a function of redshift. Using our selected sample of zCOSMOS spectra, we determine the median line flux ratios of [S II]λ6716/H$\alpha = 0.13$ and [S II]λ6731/H$\alpha = 0.10$. In the initial calculation, we neglect the [N II] doublet, as it is rarely detected with confidence in the zCOSMOS spectra, and instead correct for [N II] contamination in our final overall calibration (see below). We then covert to a line luminosity using standard luminosity distance in our assumed cosmology. To account for the unknown redshifts of the purely photometric Hα sources, we compute the average luminosity of each source over the redshift range $z = 0.3$–0.42, taking into account the different luminosity distances and filter transmission efficiencies as a function of redshift.

We compute the fluxes of the [O III]λ5007,4959 and Hβ lines in a similar manner. We assume a flux ratio of 3:1 in the [O III] doublet, and we adopt [O III]λ5007/H$\beta = 2.52$ based on the median of our selected sample of zCOSMOS spectra. We again show the full calculation in the Appendix.

We verify the accuracy of these line flux calculations using the selected zCOSMOS sample. We first flux calibrate the zCOSMOS spectra by integrating the spectra through the broadband-filter bandpasses and renormalizing the spectra to match the fluxes measured in the HSC photometry. We then extract line fluxes from the spectra by fitting Gaussians to two groups of lines: (1) Hβ and [O III]$\lambda\lambda$4959,5007; and (2) Hα, [N II]$\lambda\lambda$6548,6583, and [S II]λ6716, 6731 (if available in the spectral range). We fit each group's lines simultaneously, using multiple Gaussians of the same width with fixed ratios of the line centers to account for any minor errors in the reported spectroscopic redshifts. We use the integrated areas of the fixed Gaussians as the line flux measurements. We then compare these fitted line fluxes to our broadband-derived line fluxes.

For HAEs, the broadband method overestimates the line flux by 6.3% relative to the median, so we rescale our broadband-derived Hα fluxes down by the same 6.3% to compensate for the offset. We attribute this rescaling to contamination from the [N II] doublet, which is rarely detected with confidence in most spectra. After this rescaling, the distribution of errors $(\log(F_{\mathrm{H}\alpha,\mathrm{phot}}) - \log(F_{\mathrm{H}\alpha,\mathrm{spec}}))$ is roughly symmetric with a standard deviation of 0.159 and shows no correlation with the measured line luminosity. Thus, on average, our broadband-derived Hα line fluxes are accurate to within $\sim$37%.

For O3Es, the broadband method underestimates the line flux by 29% relative to the median, so we again apply an appropriate rescaling. We expect that this offset is due to some contamination of the continuum levels in the *i* and *Y*bands by other emission lines, such as [O III]λ4363 and Hγ, as well as underlying continuum shape effects. The resulting distribution of errors $(\log(F_{[O\mathrm{III}],\mathrm{phot}}) - \log(F_{[O\mathrm{III}],\mathrm{spec}}))$ is also roughly symmetric and uncorrelated with the measured line luminosity. The distribution has a standard deviation of 0.125, indicating an average [O III]λ5007 flux accuracy of $\sim$30%.

We attribute the scatter and initial offsets on these measurements to the inherent uncertainties in deriving line fluxes from a broadband excess, in which parameters such as line ratios and continuum slopes/shapes cannot be determined. For instance, we calculate the assumed fixed line ratios from the median of the spectroscopic sample, which may not be accurate for an individual source. Despite this, due to the symmetries of the error distributions and the lack of correlation with the measured line luminosity, these uncertainties can be largely ignored for populations of HAEs and O3Es, as the individual uncertainties will average out when considered in aggregate.

It may also be possible to derive [O III]λ5007 line luminosities at $z \sim 0.3$ from the HAE samples using the *r*-band excess. However, this may be more challenging than deriving luminosities from the *z*-band excess, as the HSC *r*filter is nearly twice as wide as the *z*filter ($\sim$1400 Å versus $\sim$760 Å), thus limiting its sensitivity to line emission by a corresponding factor of $\sim$2 and making it more susceptible to continuum effects. We intend to investigate this in a future work.

5.2. Equivalent Width Analysis

We calculate observed-frame EWs for the samples by subtracting the calculated line luminosities (Hα, [N II]$\lambda\lambda$6548, 6583, and [S II]$\lambda\lambda$6716, 6731 for HAEs; and [O III]$\lambda\lambda$4959, 5007, and Hβ for O3Es) from the total *z*-filter flux to determine a local continuum level. We then divide the derived line luminosities by their corresponding continuum levels. We again verify the accuracy of these results by comparing to the fitted zCOSMOS lines fluxes and EWs. The distributions of errors on the estimated photometric EWs $(\log(\mathrm{EW}_{\mathrm{phot}}) - \log(\mathrm{EW}_{\mathrm{spec}}))$ are roughly symmetric and centered on zero for both HAEs and O3Es.

We show the distributions of observed-frame EWs for HAEs and O3Es in COSMOS and HEROES in Figure 6. The medians for HAEs are 64 Å and 65 Å (rest-frame 47 Å and 48 Å), respectively. Both HAE distributions cut off at 16 Å, the minimum observed-frame EW permitted by our color cuts, and have extended tails to high EW. At the very high-EW end, many of these sources may be spurious; however, they may also be good candidates for studies of the most extreme star-forming galaxies or AGN. The O3E EW medians are 86 Å and 96 Å (rest-frame 48 Å and 54 Å), respectively. The O3E distributions have very similar shapes to the HAE distributions, with low-end cutoffs at 19 Å and extended high-EW tails. These median EWs also show broad consistency with previous measurements of EWs with redshift (e.g., Labbé et al. 2013, their Figure 5).

5.3. Contamination Corrections

As demonstrated in Figure 4, our spectroscopic samples are 94% EELGs. In constructing LFs from the photometric samples, we corrected the samples to account for this $\sim$6% contamination fraction. We performed this correction as a function of line luminosity, calculating the fraction of spectroscopic sources that are both photometrically and spectroscopically identified as HAEs or O3Es for each luminosity bin and rescaling the photometric LF by this purity fraction. By calculating this fraction, we implicitly require spectroscopic coverage in each luminosity bin, thus ensuring reliable photometric luminosity calibration at all the luminosities of interest.

5.4. AGN Correction

We expect our *z*-excess samples to be contaminated by AGN. We attempted to correct for this contamination by producing a Baldwin, Phillips, & Terlevich (BPT) diagram

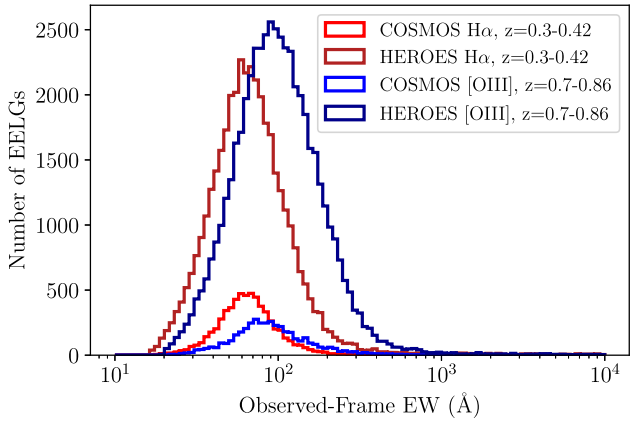

Figure 6. Distributions of observed-frame EWs for HAEs and O3Es in COSMOS and HEROES. The histogram bins are equal width (0.05 log Å) in log space and are consistent between all four curves.

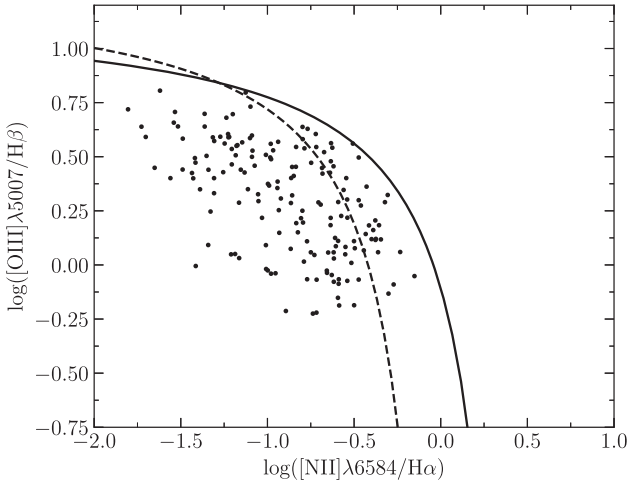

Figure 7. BPT diagram constructed from the highest-S/N subsample of the selected zCOSMOS sample. The dashed curve is the Kauffmann et al. (2003) empirical demarcation, and the solid black curve is the theoretical Kewley et al. (2001) line.

(Baldwin et al. 1981) for the selected zCOSMOS sample, which we restricted to 232 sources that passed signal-to-noise cuts on the [N II] line (see Figure 7). Despite consisting of only the highest-S/N objects in the selected zCOSMOS sample, we found the star-forming track of the BPT diagram to be quite noisy and thus unreliable for differentiating the star-forming galaxies from AGN. This noisy BPT diagram has been seen in previous studies and seems to be inherent in the zCOSMOS data set (e.g., Bongiorno et al. 2010, their Figure 3). The issue of AGN rejection via the BPT diagram is further complicated by the low signal-to-noise of the [N II]λ6584 line in fainter sources, and by the rarity of bright sources.

In a similar Hα study using a narrowband filter (CFHT/WIRcam LowOH2, center $\sim$11,870 Å), Sobral et al. (2013, 2015, 2016) faced similar challenges with rejecting AGN, and they ultimately adopted the constant AGN-contamination fractions of 10% at redshift $z = 0.4$ and 15% at redshift $z = 0.84$ up to $L \sim L^*$, based on C-COSMOS X-ray data (Elvis et al. 2009) and archival Spitzer/IRAC data. Above L^*, they observed steep increases (AGN fraction $=0.38\log(L_{H\alpha}) - 15.8$) based on spectroscopic follow-up of their most luminous identified HAEs at $z = 0.8$.

We adopted their results in correcting our own Hα LF, taking $L^* = 10^{42}$ erg s^{-1} as the dividing value between the constant and linear corrections.

5.5. Completeness Correction

We utilized Monte Carlo simulations to test the photometric completeness of our samples. We selected a star-forming galaxy template spectrum (`graz01_00050.dat`) from the `EAZY` photometric redshift fitting code (Brammer et al. 2008), which was based on the `PEGASE.2` galaxy spectral synthesis code (Fioc & Rocca-Volmerange 1999). We removed the emission lines from the template to produce a continuum model. We then modeled the Hα, Hβ, Hγ, [OII]λ3727, [O III] λ5007,4959,4363, and [N II]λ6583,6548 emission lines as 1D Gaussians and inserted them into the model spectrum, varying the redshift, Hα luminosity, and Hα EW. To determine the other line luminosities, we used the case B ratio for Hβ and Hγ, and the median ratios in the spectroscopic sample of line fluxes to the Hα line fluxes for nonhydrogen lines. To account for reddening, we calibrated and applied the Calzetti et al. (2000) extinction law to the rest-frame spectra using an attenuation of Hα of $A_{\rm H\alpha} = 1.0$ mag, as is commonly assumed in the literature (e.g., Hopkins 2004; Takahashi et al. 2007; Sobral et al. 2013, 2015; Matthee et al. 2017). We chose the Calzetti et al. (2000) extinction law for its applicability to star-forming galaxies. Moreover, at rest-frame wavelengths $\lambda \gtrsim 3000$ Å, most extinction curves (e.g., LMC, SMC, and Calzetti et al. 2000) offer similar optical-NIR slopes such that differences would only be appreciable in the observed-frame *g*filter (Salim & Narayanan 2020).

We simulated HAE spectra for all the permutations of $\log(L_{\rm H\alpha}) = 40.50, 40.75, 42.00, \ldots 43.00$ erg s^{-1}, $z = 0.300$, 0.325, 0.350, ... 0.425, and rest-frame $\rm EW_{H\alpha} = 30$, 40, 50, 75, 100, 125, 150 Å. We similarly simulated O3E spectra for all the permutations of $\log(L_{[O\,III]}) = 41.00$, 41.25, 41.50, ... 43.00 erg s^{-1}, $z = 0.700$, 0.725, 0.750, ... 0.875, and rest-frame $\rm EW_{[O\ III]} = 30$, 40, 50, 75, 100, 125, 150 Å.

We produced artificial HAEs and O3Es from these model spectra as 2D Gaussian point sources with a FWHM of 0″.9, which is the median of the photometric data set. We derived broadband magnitudes for these sources by integrating over the model spectra and *grizY*filter response curves. We then converted the simulated broadband magnitudes into imaging counts based on the stacked imaging zero-point and effective exposure time. We used these counts to set the amplitude of the 2D Gaussian source models. For each model spectrum, we inserted artificial sources in the processed HEROES and COSMOS imaging (in *g*, *r*, *i*, *z*, *Y*), corresponding to a simulated source density of $\sim$1 arcmin^{-2}, which is sufficient to well sample the imaging with minimal source-source overlap. We used `sep` (Barbary 2016), a Python derivative of `SExtractor` (Bertin & Arnouts 1996), to detect sources in the *z*filter with a 5σ detection threshold and to measure forced aperture magnitudes for the detected sources in *g*, *r*, *i*, *z*, *Y*. We then applied our photometric selection cuts to the resulting source catalog and determined which fraction of the simulated sources we recovered. We took this fraction as our completeness value for the combination of the given redshift, Hα or [O III] EW, and Hα or [O III] luminosity.

In Figure 8, we show the completeness averaged over the chosen redshift ranges (HAEs: $0.30 < z < 0.42$, O3Es: $0.70 < z < 0.86$) and over the rest-frame EWs seen in the

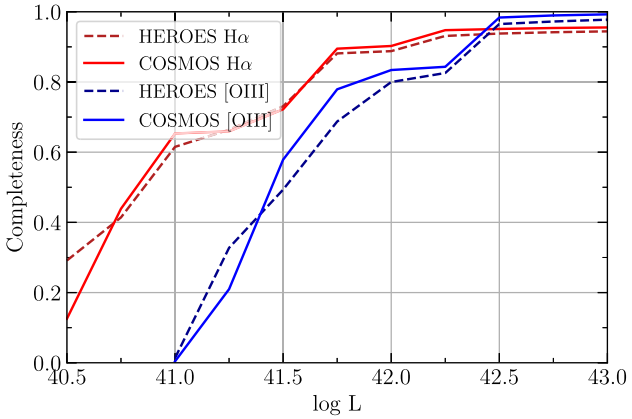

Figure 8. Average completeness of the photometric HAE (red) and O3E (blue) samples for both HEROES (dashed) and COSMOS (solid) fields.

selected zCOSMOS spectral catalog as a function of line luminosity. As expected, the COSMOS field's superior imaging quality offers marginally higher completeness at the bright end for both species. We assume ±10% error on our completeness at all luminosities to account for any minor effects from our choice of spectral template, simulated line ratios, and dust-attenuation law.

5.6. Luminosity Functions

Figures 9 and 10 show the photometric Hα and [O III] LFs. We provide the data from these figures in Table 2. Our comoving volumes are calculated from the 3.15/34.2 deg^2 observed areas (COSMOS/HEROES), and the redshift ranges $0.30 < z < 0.42$ and $0.70 < z < 0.86$. The COSMOS field has a comoving volume of 8.15×10^5 Mpc^3 at $0.30 < z < 0.42$, and 3.17×10^6 Mpc^3 at $0.70 < z < 0.86$. HEROES encompasses 8.85×10^6 Mpc^3 at $0.30 < z < 0.42$, and 3.44×10^7 Mpc^3 at $0.70 < z < 0.86$.

As described above, we correct our Hα LFs for completeness (via the completeness simulations), for sample purity (using the fraction of positive spectroscopic confirmations at a given luminosity), and for AGN contamination (using the prescription from Sobral et al. 2015). We cut off our LFs at the faint end, ignoring the luminosity bins with <50% completeness. We characterize our uncertainties assuming simple Poissonian statistics ($\sigma_x = \sqrt{x}$) for the populations of photometric candidates, spectroscopically confirmed HAEs or O3Es, and spectroscopically blank/indeterminate objects for each luminosity bin. We propagate these errors, along with an assumed 10 percentage point error on the completeness correction, to produce our plotted 1σ error bars. As a result, our LF uncertainties are a function of both the number of photometric sources in a bin (which scales with survey area) and the spectroscopic completeness of each sample. Thus, due to its much higher spectroscopic completeness (13.8% verses 0.39%), our COSMOS Hα LF has smaller uncertainties than HEROES Hα LF, despite HEROES' ∼10x larger comoving volume.

Up to $\log(L_{H\alpha}) = 42.0$ erg s^{-1}, the COSMOS Hα LF exhibits a ∼0.3 dex offset from the HEROES Hα LF. We attribute this offset to the aforementioned differences in the data quality between the two data sets, to any photometric calibration offsets between the two data sets, and to cosmic variance. Using the methodology of Driver & Robotham (2010), we estimate the cosmic variance in our surveyed Hα-sensitive COSMOS and HEROES volumes of 20% and 10%,

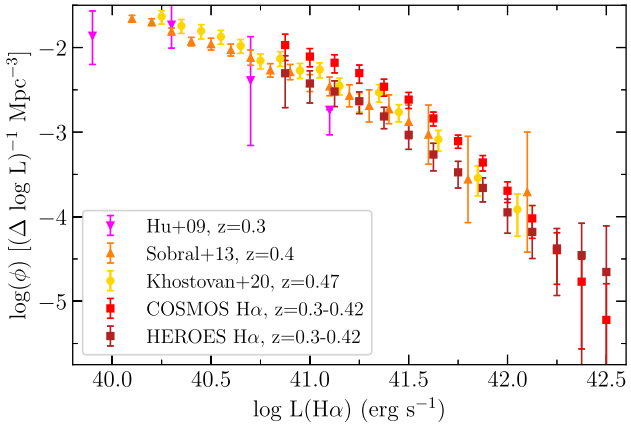

Figure 9. Incompleteness and AGN-corrected photometric LFs for Hα at $0.30 < z < 0.42$ (COSMOS: red squares; HEROES: dark-red squares) and literature samples (see figure legend). Note that none of the LFs shown correct for dust attenuation (the dust-attenuation adjustment of 1 magnitude has been removed from the Sobral et al. (2013) data set). The Hu et al. (2009) data set has been scaled up by a factor of 25 to account for their limited selection of USELs (see Hu et al. 2009, their Figure 14 for details). We provide the data in this figure in Table 2.

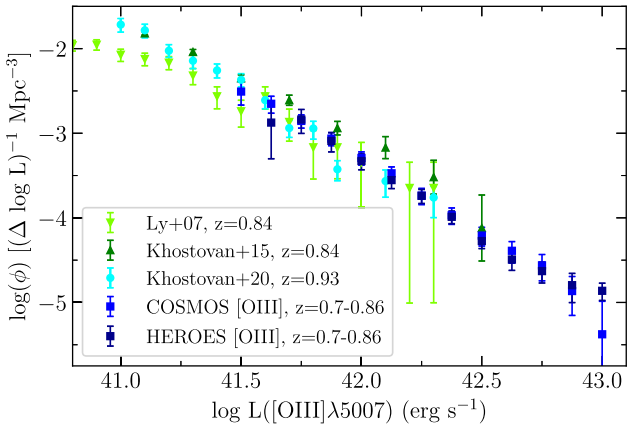

Figure 10. Incompleteness-corrected photometric LFs for [O III] at $0.70 < z < 0.86$ (COSMOS: blue squares, HEROES: dark-blue squares) and literature samples (see figure legend). Note that none of the LFs shown are corrected for dust attenuation and that the Khostovan et al. (2015) data are for a combined [O III]+Hβ LF. We provide the data in this figure in Table 2.

respectively. While these values alone are insufficient to make up the ∼0.3 dex offset, when combined with the data set to data set variance, and considering the agreement with literature samples (see below), we are unconcerned by this offset.

We compare our Hα LFs to literature samples from Hu et al. (2009; pink downward triangles), Sobral et al. (2013; orange upward triangles), and Khostovan et al. (2020; yellow circles). All of these samples were selected from narrowband imaging surveys (NB816 and NB921; NB921 and NB964, respectively) and are therefore more sensitive to line emission than our broadband selection, while probing correspondingly smaller comoving volumes due to the inherently narrow passbands. Given the ∼800 Å width of the $z$filter compared to the ∼120 Å width of the narrowband filters, our selection probes ∼6x the comoving volume of a narrowband study for an equivalent survey area at the cost of a corresponding ∼6x increase in the uncertainty on the redshifts of photometric candidates.

It is important to note that none of the plotted LFs are corrected for dust attenuation. Sobral et al. (2013) assumed (as

Table 2
Luminosity Function Data

$\log L$ (erg s^{-1})	COSMOS $\log \Phi_{H\alpha}$	HEROES $\log \Phi_{H\alpha}$	COSMOS $\log \Phi_{[OIII]}$	HEROES $\log \Phi_{[OIII]}$
		($\Delta \log L^{-1}$ Mpc^{-3})		
40.875	$-1.971^{+0.128}_{-0.183}$	$-2.304^{+0.206}_{-0.407}$	…	…
41.000	$-2.107^{+0.094}_{-0.121}$	$-2.425^{+0.150}_{-0.231}$	…	…
41.125	$-2.180^{+0.094}_{-0.120}$	$-2.520^{+0.126}_{-0.178}$	…	…
41.250	$-2.302^{+0.095}_{-0.121}$	$-2.635^{+0.109}_{-0.147}$	…	…
41.375	$-2.463^{+0.089}_{-0.112}$	$-2.815^{+0.108}_{-0.144}$	…	…
41.500	$-2.616^{+0.085}_{-0.106}$	$-3.032^{+0.123}_{-0.172}$	$-2.507^{+0.116}_{-0.160}$	…
41.625	$-2.838^{+0.074}_{-0.090}$	$-3.265^{+0.133}_{-0.193}$	$-2.652^{+0.089}_{-0.111}$	$-2.874^{+0.211}_{-0.427}$
41.750	$-3.107^{+0.071}_{-0.085}$	$-3.475^{+0.130}_{-0.186}$	$-2.854^{+0.071}_{-0.085}$	$-2.838^{+0.119}_{-0.164}$
41.875	$-3.359^{+0.082}_{-0.101}$	$-3.660^{+0.119}_{-0.165}$	$-3.064^{+0.070}_{-0.084}$	$-3.091^{+0.100}_{-0.129}$
42.000	$-3.694^{+0.105}_{-0.139}$	$-3.949^{+0.156}_{-0.247}$	$-3.292^{+0.071}_{-0.085}$	$-3.329^{+0.084}_{-0.103}$
42.125	$-4.020^{+0.152}_{-0.236}$	$-4.181^{+0.180}_{-0.314}$	$-3.473^{+0.076}_{-0.092}$	$-3.554^{+0.082}_{-0.100}$
42.250	$-4.396^{+0.206}_{-0.404}$	$-4.376^{+0.236}_{-0.556}$	$-3.737^{+0.085}_{-0.106}$	$-3.74^{+0.075}_{-0.090}$
42.375	$-4.769^{+0.265}_{-0.796}$	$-4.455^{+0.378}_{-\infty}$	$-3.969^{+0.086}_{-0.108}$	$-3.988^{+0.068}_{-0.081}$
42.500	$-5.221^{+0.428}_{-\infty}$	$-4.654^{+0.545}_{-\infty}$	$-4.209^{+0.096}_{-0.124}$	$-4.274^{+0.074}_{-0.089}$
42.625	…	…	$-4.389^{+0.109}_{-0.145}$	$-4.493^{+0.099}_{-0.128}$
42.750	…	…	$-4.562^{+0.128}_{-0.183}$	$-4.629^{+0.106}_{-0.141}$
42.875	…	…	$-4.865^{+0.172}_{-0.288}$	$-4.796^{+0.139}_{-0.206}$
43.000	…	…	$-5.376^{+0.390}_{-\infty}$	$-4.862^{+0.090}_{-0.114}$

is common in the literature; see also Khostovan et al. (2020), their Section 3.4, and references therein) a 1 magnitude attenuation of the Hα line flux. We remove this correction in Figure 9 by offsetting the Sobral et al. (2013) data set by -0.4 dex from their reported luminosity values. While we considered performing a dust-attenuation correction of our own data, we found that our spectroscopic data sets were insufficiently calibrated to provide reliable Hα/ Hβ line ratios for calibrating dust attenuation with the Balmer decrement. Khostovan et al. (2020) noted the same difficulty with the zCOSMOS data set and instead opted for a dust correction based on $g-r$ colors. We refrained from using such a correction to avoid any potential bias introduced by using $g-r$ color for both dust attenuation and differentiation between HAEs and O3Es.

Hu et al. (2009) reported that their USEL LF offered agreement with the more general Hα LF of Tresse & Maddox (1998) if the general LF were multiplied by 0.04. We thus scale up the Hu et al. (2009) data by a factor of 25 to compensate for this effect and to provide a direct comparison to the other studies.

With these adjustments applied, we find that the HEROES Hα LF is within the 1σ error bounds of the other studies. The offset on the COSMOS Hα LF marginally separates it from the other studies, but when cosmic variance and the different redshift intervals are taken into consideration, this LF is still in agreement with the literature samples. From these results, we conclude that our 5-broadband z-excess selection technique is reliable and well-calibrated for selecting HAEs at $0.30 < z < 0.42$.

We construct our [O III] LFs in much the same way as the Hα LFs, except that we do not include an AGN-contamination correction. This allows us to make a more direct comparison with the other studies that also lack an AGN correction, such as Khostovan et al. (2020). In contrast to the Hα LFs, our COSMOS and HEROES [O III] LFs show remarkable agreement with one another, with a median offset of 0.02 dex. Both LFs show strong agreement within the error bounds of the narrowband-selected literature samples from Ly et al. (2007; light-green downward-pointing triangles) and Khostovan et al. (2020; cyan circles). The data from Khostovan et al. (2015; dark-green upward-pointing triangles) are a combined [O III] +Hβ LF, which may explain the slight offset from the other studies around $\log(L_{[OIII]}) = 42.0$ erg s^{-1}. Due to the lack of AGN corrections, all of the studies deviate from a Schechter-like shape above $\log(L_{[OIII]}) \sim 41.75$ erg s^{-1}. Due to the large comoving volumes sampled by our broadband selection, our LFs are able to push to $\log(L_{[OIII]}) = 43.0$ erg s^{-1}, brighter than any of the literature studies. At this bright end, the LFs strongly resemble a power law and are likely dominated by contributions from AGN. We intend to investigate the AGN contribution at $z \sim 0.7$ in a future study. Due to our decreased line sensitivity when compared to narrowband surveys and our corresponding $Y < 23$ constraint to ensure strong photometric detections, we do not probe as faint as the narrowband literature studies, but we nonetheless demonstrate the reliability of our broadband-selection method.

This result is particularly exciting in the context of VRO. Over its 10 yr main survey, VRO expects to reach 5σ imaging depths of 25.8, 27.0, 27.2, 27.0, 25.7, and 24.4 for *ugrizy*, respectively, over ~18,000 deg^2 (LSST Science Collaboration 2009). These depths are all equal to or deeper than our requirements of *g*,*r*,*i*, $z < 25$, and $y < 23$ and will likely meet our requirements by the end of the first survey year (assuming uniform coverage in all filters and efficient data processing). Using our selection cuts, and scaling from the number density of sources in the NEP, we expect that VRO may detect ~21 million HAEs at $0.30 < z < 0.42$ and ~28 million O3Es at $0.70 < z < 0.86$. Thus, VRO-EELG studies may very easily constrain the bright end of the LFs, subject to suitable AGN rejection. As with our COSMOS and HEROES samples, the VRO data will need to be carefully calibrated with spectroscopic measurements of sources across its survey field to both inform its exact color and magnitude cuts and constrain contamination levels in the photometric EELG samples. Whether analyzed as a contiguous ~18,000 deg^2 or more practically in smaller segments, VRO will reveal an unprecedented number of HAEs and O3Es with the z-excess method.

6. Conclusions

The main results of our work are as follows:

1. We introduced a novel z-excess 5-filter broadband-selection technique for identifying HAEs at $0.3 < z < 0.42$ and O3Es at $0.7 < z < 0.86$.
2. Using 3.15 deg^2 of HSC-SSP broadband data in the COSMOS field in conjunction with archival spectroscopic data from zCOSMOS and DEIMOS 10K, as well as new observations from WIYN/HYDRA, we tested this selection technique.
3. We expanded and applied the technique to 34.2 deg^2 of HEROES broadband data in the NEP field and new spectroscopy from Keck/DEIMOS and WIYN/HYDRA.
4. We presented spectroscopic catalogs of HAEs and O3Es identified in our WIYN/HYDRA observations (see Appendix).
5. We introduced analytical expressions for estimating Hα or [O III] line flux from broadband magnitudes, and we calibrated the expressions using the spectroscopic data sets.
6. Using our broadband-selection technique and calibrated line flux expressions, we constructed Hα and [O III] LFs

and found strong agreement with narrowband literature studies.

Based on the 94% fidelity in selecting spectroscopic HAEs and O3Es, the 98.5% accuracy in differentiating them from each other, and the strong agreement with literature LFs, we conclude that the z-excess 5-filter broadband-selection technique presented in this work is both accurate and effective in identifying EELGs at $z < 1$ either for spectroscopic follow-up in small fields or for population analysis in large fields, without the need for costly full-spectroscopic samples. With the ever increasing sizes of current and future multiband photometric surveys, such as those that will be obtained with the VRO, this technique may be the key to identifying and characterizing unprecedented numbers of EELGs in a straightforward manner.

We thank the anonymous referee for an insightful report that helped us to improve this work. We gratefully acknowledge support for this research from Jeff and Judy Diermeier through a Diermeier Fellowship (B.E.R.), a Wisconsin Space grant Consortium Graduate and Professional Research Fellowship (A.J.T.), a Sigma Xi Grant in Aid of Research (A.J.T.), NSF grants AST-1716093 (E.M.H., A.S.) and AST-1715145 (A.J.B.), the William F. Vilas Estate and a Kellett Mid-Career Award and a WARF Named Professorship from the University of Wisconsin-Madison Office of the Vice Chancellor for Research and Graduate Education with funding from the Wisconsin Alumni Research Foundation (A.J.B.).

This paper is based in part on data collected from the Subaru Telescope. The Hyper Suprime-Cam (HSC) collaboration includes the astronomical communities of Japan and Taiwan, and Princeton University. The HSC instrumentation and software were developed by the National Astronomical Observatory of Japan (NAOJ), the Kavli Institute for the Physics and Mathematics of the Universe (Kavli IPMU), the University of Tokyo, the High Energy Accelerator Research Organization (KEK), the Academia Sinica Institute for Astronomy and Astrophysics in Taiwan (ASIAA), and Princeton University. Funding was contributed by the FIRST program from Japanese Cabinet Office, the Ministry of Education, Culture, Sports, Science and Technology (MEXT), the Japan Society for the Promotion of Science (JSPS), Japan Science and Technology Agency (JST), the Toray Science Foundation, NAOJ, Kavli IPMU, KEK, ASIAA, and Princeton University.

This paper also makes use of data collected at the Subaru Telescope and retrieved from the HSC data archive system, which is operated by Subaru Telescope and Astronomy Data Center at National Astronomical Observatory of Japan. Data analysis was in part carried out with the cooperation of Center for Computational Astrophysics, National Astronomical Observatory of Japan.

This paper is based in part on data collected from the Keck II Telescope. The W. M. Keck Observatory is operated as a scientific partnership among the California Institute of Technology, the University of California, and NASA, and was made possible by the generous financial support of the W. M. Keck Foundation.

This work is based in part on observations at Kitt Peak National Observatory, NSF's National Optical-Infrared Astronomy Research Laboratory, which is operated by the Association of Universities for Research in Astronomy (AURA) under a cooperative agreement with the National Science Foundation. The WIYN Observatory is a joint facility of the NSF's National Optical-Infrared Astronomy Research Laboratory, Indiana University, the University of Wisconsin-Madison, Pennsylvania State University, the University of Missouri, the University of California-Irvine, and Purdue University.

This material is based upon work supported by NASA under Award No. RFP20_9.0 issued through Wisconsin Space Grant Consortium. Any opinions, findings, and conclusions or recommendations expressed in this material are those of the authors and do not necessarily reflect the views of the National Aeronautics and Space Administration.

This research made use of *Astropy*, a community-developed core Python package for Astronomy (Astropy Collaboration et al. 2013, 2018).

The authors wish to recognize and acknowledge the important cultural role and reverence that the summit of Maunakea has always had within the Hawaiian community. We are fortunate to have the opportunity to conduct observations from this site.

Appendix

Here we show the derivation of an estimated Hα line luminosity from the *i*-, *z*-, and *Y*-broadband fluxes, the corresponding broadband-filter transmission curves, and an assumed redshift (see Section 5.1).

Assume that the continuum flux density in the z filter, z_c, is as follows:

$$z_c = (i_c + y_c)/2. \tag{1}$$

In the detected redshift range, Hα must be in the *z*filter to cause a *z*-excess detection, but the [S II] doublet may fall in the neighboring *Y*filter. The flux density in each filter is given by

$$i = i_c, \tag{2}$$

$$z = z_c + \frac{\epsilon_{z\mathrm{H}\alpha}\mathrm{H}\alpha + \epsilon_{z6716}[SII]_{6716} + \epsilon_{z6731}[SII]_{6731}}{\Delta\lambda_z}, \tag{3}$$

$$\text{and } y = y_c + \frac{\epsilon_{y6716}[SII]_{6716} + \epsilon_{y6731}[SII]_{6731}}{\Delta\lambda_y}. \tag{4}$$

Here, x_c is the continuum flux density in filter x, $\Delta\lambda_x$ is the effective width of filter x; Hα, $[\mathrm{S\,II}]_{6716}$, $[\mathrm{S\,II}]_{6731}$ are the integrated observed-frame line fluxes of Hα, $[\mathrm{S\,II}]_{6716}$, $[\mathrm{S\,II}]_{6731}$, respectively, and ϵ_{xn} is the filter efficiency of filter x at wavelength n.

We next assume constant line flux ratios of $[\mathrm{S\,II}]_{6716}/\mathrm{H}\alpha = 0.13$ and $[\mathrm{S\,II}]_{6731}/\mathrm{H}\alpha = 0.10$. Inserting this substitution and simplifying gives

$$z = z_c + (\epsilon_{z\mathrm{H}\alpha} + 0.13\epsilon_{z6716} + 0.10\epsilon_{z6731})\frac{\mathrm{H}\alpha}{\Delta\lambda_z}, \tag{5}$$

$$y = y_c + (0.13\epsilon_{y6716} + 0.10\epsilon_{y6731})\frac{\mathrm{H}\alpha}{\Delta\lambda_y}. \tag{6}$$

Multiplying (1) by a factor of two and plugging (2, 5, and 6) into (1) gives

$$2z - 2(\epsilon_{z\mathrm{H}\alpha} + 0.13\epsilon_{z6716} + 0.10\epsilon_{z6731}) \times \frac{\mathrm{H}\alpha}{\Delta\lambda_z} = i + y - (0.13\epsilon_{y6716} + 0.10\epsilon_{y6731})\frac{\mathrm{H}\alpha}{\Delta\lambda_y}. \tag{7}$$

Collecting like terms gives

$$i + y - 2z = \mathrm{H}\alpha\left[\frac{0.13\epsilon_{y6716} + 0.10\epsilon_{y6731}}{\Delta\lambda_y} - \frac{2(\epsilon_{z\mathrm{H}\alpha} + 0.13\epsilon_{z6716} + 0.10\epsilon_{z6731})}{\Delta\lambda_z}\right] \quad (8)$$

$$\mathrm{H}\alpha = \frac{i + y - 2z}{\frac{0.13\epsilon_{y6716}+0.10\epsilon_{y6731}}{\Delta\lambda_y} - \frac{2(\epsilon_{z\mathrm{H}\alpha}+0.13\epsilon_{z6716}+0.10\epsilon_{z6731})}{\Delta\lambda_z}}. \quad (9)$$

With d_L as the redshift-determined luminosity distance of the [O III]$_{5007}$ source, the rest-frame [O III]$_{5007}$ luminosity (L) is given by

$$L = 4\pi d_L^2 \mathrm{H}\alpha = \frac{4\pi d_L^2 (i + y - 2z)}{\frac{0.13\epsilon_{y6716}+0.10\epsilon_{y6731}}{\Delta\lambda_y} - \frac{2(\epsilon_{z\mathrm{H}\alpha}+0.13\epsilon_{z6716}+0.10\epsilon_{z6731})}{\Delta\lambda_z}}. \quad (10)$$

For the special case in which all three lines fall within z, $\epsilon_y = 0$ and $\epsilon_i = 0$ for all lines, greatly simplifying the expression to

$$L = 4\pi d_L^2 \mathrm{H}\alpha = \frac{4\pi d_L^2 (z - \frac{i+y}{2})\Delta\lambda_z}{(\epsilon_{z\mathrm{H}\alpha} + 0.13\epsilon_{z6716} + 0.10\epsilon_{z6731})}. \quad (11)$$

Here we now show the derivation of an estimated [O III] λ5007 line luminosity from the i-, z-, and Y-broadband fluxes, the corresponding broadband-filter transmission curves, and an assumed redshift (see Section 5.1).

Assume that the continuum flux density in the z filter, z_c, is as follows:

$$z_c = (i_c + y_c)/2. \quad (12)$$

In the detected redshift range, [O III]$_{5007}$ must fall in the $z$filter to cause a z-excess detection, but Hβ and/or [O III]$_{4959}$ may fall in the neighboring i-filter. This can be mitigated by modifying the redshift range to require that all three lines fall in z (see simplified special case at the end). The flux density in each filter is given by

$$i = i_c + \frac{\epsilon_{iH\beta} H\beta + \epsilon_{i4959}[\mathrm{O\ III}]_{4959}}{\Delta\lambda_i}, \quad (13)$$

$$z = z_c + \frac{\epsilon_{zH\beta} H\beta + \epsilon_{z4959}[\mathrm{O\ III}]_{4959} + \epsilon_{z5007}[\mathrm{O\ III}]_{5007}}{\Delta\lambda_z}, \quad (14)$$

$$\text{and } y = y_c. \quad (15)$$

Here, x_c is the continuum flux density in filter x, $\Delta\lambda_x$ is the effective width of filter x, $H\beta$, [O III]$_{4959}$, [O III]$_{5007}$ are the integrated observed-frame line fluxes of $H\beta$, [O III]$_{4959}$, [O III]$_{5007}$, respectively, and ϵ_{xn} is the filter efficiency of filter x at wavelength n.

We next assume constant line flux ratios of [O III]$_{4959}$/[O III]$_{5007} = 0.33$ and $H\beta$/[O III]$_{5007} = 0.40$ in order to have all of the line fluxes in terms of [O III]$_{5007}$. Inserting this substitution and simplifying gives

$$i = i_c + (0.40\epsilon_{iH\beta} + 0.33\epsilon_{i4959})\frac{[\mathrm{O\ III}]_{5007}}{\Delta\lambda_i}, \quad (16)$$

$$z = z_c + (0.40\epsilon_{zH\beta} + 0.33\epsilon_{z4959} + \epsilon_{z5007})\frac{[\mathrm{O\ III}]_{5007}}{\Delta\lambda_z}. \quad (17)$$

Multiplying (12) by a factor of two and plugging (15, 16, and 17) into (12) gives

$$2z - 2(0.40\epsilon_{zH\beta} + 0.33\epsilon_{z4959} + \epsilon_{z5007}) \times \frac{[\mathrm{O\ III}]_{5007}}{\Delta\lambda_z} = i - (0.40\epsilon_{iH\beta} + 0.33\epsilon_{i4959}) \times \frac{[\mathrm{O\ III}]_{5007}}{\Delta\lambda_i} + y \quad (18)$$

Collecting like terms gives

$$i + y - 2z = [\mathrm{O\ III}]_{5007}\left[\frac{0.40\epsilon_{iH\beta} + 0.33\epsilon_{i4959}}{\Delta\lambda_i} \times -2\frac{0.40\epsilon_{zH\beta}/ + 0.33\epsilon_{z4959} + \epsilon_{z5007}}{\Delta\lambda_z}\right] \quad (19)$$

$$[\mathrm{O\ III}]_{5007} = \frac{i + y - 2z}{\frac{0.40\epsilon_{iH\beta}+0.33\epsilon_{i4959}}{\Delta\lambda_i} + -\frac{2(0.40\epsilon_{zH\beta}+0.33\epsilon_{z4959}+\epsilon_{z5007})}{\Delta\lambda_z}}. \quad (20)$$

With d_L as the redshift-determined luminosity distance of the [O III]$_{5007}$ source, the rest-frame [O III]$_{5007}$ luminosity (L) is given by

$$L = 4\pi d_L^2 [\mathrm{O\ III}]_{5007} = \frac{4\pi d_L^2 (i + y - 2z)}{\frac{0.40\epsilon_{iH\beta}+0.33\epsilon_{i4959}}{\Delta\lambda_i} - \frac{2(0.40\epsilon_{zH\beta}+0.33\epsilon_{z4959}+\epsilon_{z5007})}{\Delta\lambda_z}}. \quad (21)$$

For the special case in which all three lines fall within z, $\epsilon_i = 0$ for all lines, greatly simplifying the expression to

$$L = 4\pi d_L^2 [\mathrm{O\ III}]_{5007} = 4\pi d_L^2 \frac{z - \frac{i+y}{2}}{0.40\epsilon_{zH\beta} + 0.33\epsilon_{z4959} + \epsilon_{z5007}}\Delta\lambda_z. \quad (22)$$

ORCID iDs

Anthony J. Taylor https://orcid.org/0000-0003-1282-7454
Amy J. Barger https://orcid.org/0000-0002-3306-1606
Lennox L. Cowie https://orcid.org/0000-0002-6319-1575
Logan H. Jones https://orcid.org/0000-0002-1706-7370

References

Aihara, H., AlSayyad, Y., Ando, M., et al. 2022, PASJ, in press
Amorín, R., Pérez-Montero, E., Contini, T., et al. 2015, A&A, 578, A105
Astropy Collaboration, Price-Whelan, A. M., SipHocz, B. M., et al. 2018, AJ, 156, 123
Astropy Collaboration, Robitaille, T. P., Tollerud, E. J., et al. 2013, A&A, 558, A33
Atek, H., Siana, B., Scarlata, C., et al. 2011, ApJ, 743, 121
Baldwin, J. A., Phillips, M. M., & Terlevich, R. 1981, PASP, 93, 5
Barbary, K. 2016, JOSS, 1, 58
Bertin, E., & Arnouts, S. 1996, A&AS, 117, 393
Bongiorno, A., Mignoli, M., Zamorani, G., et al. 2010, A&A, 510, A56
Bosch, J., AlSayyad, Y., Armstrong, R., et al. 2019, in ASP Conf. Ser. 523, Astronomical Data Analysis Software and Systems XXVIII, ed. P. J. Teuben et al. (San Francisco, CA: ASP), 521
Bosch, J., Armstrong, R., Bickerton, S., et al. 2018, PASJ, 70, S5
Boyett, K. N. K., Stark, D. P., Bunker, A. J., Tang, M., & Maseda, M. V. 2021, arXiv:2110.15858

Brammer, G. B., van Dokkum, P. G., & Coppi, P. 2008, ApJ, 686, 1503
Calzetti, D., Armus, L., Bohlin, R. C., et al. 2000, ApJ, 533, 682
Cardamone, C., Schawinski, K., Sarzi, M., et al. 2009, MNRAS, 399, 1191
Driver, S. P., & Robotham, A. S. G. 2010, MNRAS, 407, 2131
Elvis, M., Civano, F., Vignali, C., et al. 2009, ApJS, 184, 158
Endsley, R., Stark, D. P., Charlot, S., et al. 2021, MNRAS, 502, 6044
Fioc, M., & Rocca-Volmerange, B. 1999, arXiv:astro-ph/9912179
González-Morán, A. L., Chávez, R., Terlevich, R., et al. 2019, MNRAS, 487, 4669
Grossi, M. 2018, in IAU Symp. 344, Dwarf Galaxies: From the Deep Universe to the Present, ed. K. B. W. McQuinn & S. Stierwalt (Cambridge: Cambridge Univ. Press), 319
Hasinger, G., Capak, P., Salvato, M., et al. 2018, ApJ, 858, 77
Hayashi, M., Tanaka, M., Shimakawa, R., et al. 2018, PASJ, 70, S17
Hinojosa-Goñi, R., Muñoz-Tuñón, C., & Méndez-Abreu, J. 2016, A&A, 592, A122
Hopkins, A. M. 2004, ApJ, 615, 209
Hu, E. M., Cowie, L. L., Kakazu, Y., & Barger, A. J. 2009, ApJ, 698, 2014
Hu, E. M., Cowie, L. L., Songaila, A., et al. 2016, ApJL, 825, L7
Huang, X., Zheng, W., Wang, J., et al. 2015, ApJ, 801, 12
Izotov, Y. I., Guseva, N. G., & Thuan, T. X. 2011, ApJ, 728, 161
Izotov, Y. I., & Thuan, T. X. 2016, MNRAS, 457, 64
Izotov, Y. I., Worseck, G., Schaerer, D., et al. 2021, MNRAS, 503, 1734
Kakazu, Y., Cowie, L. L., & Hu, E. M. 2007, ApJ, 668, 853
Kauffmann, G., Heckman, T. M., Tremonti, C., et al. 2003, MNRAS, 346, 1055
Kewley, L. J., Dopita, M. A., Sutherland, R. S., Heisler, C. A., & Trevena, J. 2001, ApJ, 556, 121
Khostovan, A. A., Malhotra, S., Rhoads, J. E., et al. 2020, MNRAS, 493, 3966
Khostovan, A. A., Sobral, D., Mobasher, B., et al. 2015, MNRAS, 452, 3948
Labbé, I., Oesch, P. A., Bouwens, R. J., et al. 2013, ApJL, 777, L19
Li, Z., & Malkan, M. A. 2018, ApJ, 860, 83
Lilly, S. J., Le Brun, V., Maier, C., et al. 2009, ApJS, 184, 218
LSST Science Collaboration 2009, arXiv:0912.0201
Lumbreras-Calle, A., Muñoz-Tuñón, C., Méndez-Abreu, J., et al. 2019, A&A, 621, A52
Ly, C., Malkan, M. A., Kashikawa, N., et al. 2007, ApJ, 657, 738
Magdis, G. E., Rigopoulou, D., Huang, J. S., et al. 2008, MNRAS, 386, 11
Magnier, E. A., Schlafly, E. F., Finkbeiner, D. P., et al. 2020b, ApJS, 251, 6
Magnier, E. A., Sweeney, W. E., Chambers, K. C., et al. 2020a, ApJS, 251, 5
Maseda, M. V., van der Wel, A., Rix, H.-W., et al. 2018, ApJ, 854, 29
Matthee, J., Sobral, D., Best, P., et al. 2017, MNRAS, 471, 629
Matthee, J., Sobral, D., Santos, S., et al. 2015, MNRAS, 451, 400
Miyazaki, S., Komiyama, Y., Nakaya, H., et al. 2012, Proc. SPIE, 8446, 84460Z
Naidu, R. P., Matthee, J., Oesch, P. A., et al. 2022, MNRAS, 510, 4582
Noeske, K. G., Koo, D. C., Phillips, A. C., et al. 2006, ApJL, 640, L143
Salim, S., & Narayanan, D. 2020, ARA&A, 58, 529
Sargent, W. L. W. 1970, ApJ, 160, 405
Sargent, W. L. W., & Searle, L. 1970, ApJL, 162, L155
Smit, R., Bouwens, R. J., Franx, M., et al. 2015, ApJ, 801, 122
Sobral, D., Kohn, S. A., Best, P. N., et al. 2016, MNRAS, 457, 1739
Sobral, D., Matthee, J., Best, P. N., et al. 2015, MNRAS, 451, 2303
Sobral, D., Smail, I., Best, P. N., et al. 2013, MNRAS, 428, 1128
Songaila, A., Hu, E. M., Barger, A. J., et al. 2018, ApJ, 859, 91
Takahashi, M. I., Shioya, Y., Taniguchi, Y., et al. 2007, ApJS, 172, 456
Tanaka, T. S., Shimakawa, R., Shimasaku, K., et al. 2022, PASJ, 74, 1
Tang, M., Stark, D. P., Chevallard, J., & Charlot, S. 2019, MNRAS, 489, 2572
Tang, M., Stark, D. P., Chevallard, J., et al. 2021, MNRAS, 503, 4105
Taylor, A. J., Barger, A. J., Cowie, L. L., Hu, E. M., & Songaila, A. 2020, ApJ, 895, 132
Taylor, A. J., Cowie, L. L., Barger, A. J., Hu, E. M., & Songaila, A. 2021, ApJ, 914, 79
Thuan, T. X., & Martin, G. E. 1981, ApJ, 247, 823
Tresse, L., & Maddox, S. J. 1998, ApJ, 495, 691
van der Wel, A., Straughn, A. N., Rix, H. W., et al. 2011, ApJ, 742, 111
Yang, H., Malhotra, S., Rhoads, J. E., & Wang, J. 2017, ApJ, 847, 38
Zwicky, I. F. 1964, ApJ, 140, 1467